Development and experimental validation of a low-frequency dynamic model for a Hybrid Electric Vehicle

# Development and experimental validation of a low-frequency dynamic model for a Hybrid Electric Vehicle

Kerem Koprubasi* and Giorgio Rizzoni

Center for Automotive Research,
The Ohio State University,
930 Kinnear road, Columbus, OH 43212, USA
E-mail: kkoprubasi@gmail.com
E-mail: rizzoni.1@osu.edu
*Corresponding author

Enrico Galvagno and Mauro Velardocchia

Dipartimento di Ingegneria Meccanica ed Aerospaziale,
Politecnico di Torino,
C.so Duca degli Abruzzi, 24,
Torino 10129, Italy
E-mail: enrico.galvagno@polito.it
E-mail: mauro.velardocchia@polito.it

**Abstract:** This paper describes the development and experimental validation of a high-fidelity Hybrid Electric Vehicle (HEV) simulator that enables testing and calibration of energy management and driveline control strategies. The model is capable of predicting longitudinal vehicle responses that affect energy consumption and drivability in the low-to-mid frequency region (up to 10 Hz). The simulator focuses primarily on the drivetrain dynamics, while the dynamics of the actuators are represented by simplified models. The vehicle simulator is validated by a number of experiments that include electric only, engine only and hybrid operating conditions. The test vehicle has a through-the-road parallel hybrid architecture that utilises a dual electric machine configuration. Experimental results confirm that important driveline phenomena such as shunt, shuffle, torque holes and other transient disturbances related to operating mode changes are accurately predicted.

**Keywords:** HEV; hybrid electric vehicles; powertrain modelling and control; driveline modelling; longitudinal vehicle dynamics drivability, experimental validation.

**Reference** to this paper should be made as follows: Koprubasi, K., Rizzoni, G., Galvagno, E. and Velardocchia, M. (2012) 'Development and experimental validation of a low-frequency dynamic model for a Hybrid Electric Vehicle', *Int. J. Powertrains*, Vol. 1, No. 3, pp.304–333.

**Biographical notes:** Kerem Koprubasi received his BSc in mechanical engineering from the Middle East Technical University in 2002, MSc in mechanical engineering from the University of New Hampshire in 2004 and PhD in mechanical engineering from the Ohio State University in 2008. His PhD dissertation focused on the modelling and control of hybrid drivetrains for

improved drivability during operating mode transitions. He has held research and product development positions at the GM Global R&D Centre and the GM Powertrain Headquarters between 2008 and 2011. He is currently with Ford Otosan Product Development in Turkey. His research interests include modelling and control of conventional and hybrid powertrains.

Giorgio Rizzoni, the Ford Motor Company Chair in ElectroMechanical Systems, is a Professor of mechanical and aerospace engineering at The Ohio State University (OSU). He is also Professor of electrical and computer engineering and Adjunct Professor of design. He received his PhD from the University of Michigan in 1986. Since 1999, he has been the Director of the OSU Centre for Auto-motive Research, an interdisciplinary university research centre in the OSU College of Engineering. His research interests are in energy and transportation systems, with special interest in alternative fuels and future ground vehicle propulsion systems, including advanced engines, electric and hybrid-electric drivetrains, energy storage systems and hydrogen fuel cell systems.

Enrico Galvagno (1979) graduated in mechanical engineering at Politecnico di Torino in 2004 and in 2008 he received his PhD in machines design and construction discussing a thesis on the Analysis of Automotive Transmissions with High Efficiency and Dynamic Performance. He is continuing his research at the Department of Mechanics and Aerospace Engineering in the fields of modelling, simulation, testing and control of automotive transmission systems as a post-doctoral fellow. He is currently a member of the vehicle dynamics and active safety systems research group.

Mauro Velardocchia (1963) is a Full Professor of applied mechanics. He is the Founder (1998) of the Politecnico di Torino's (PoliTO) vehicle dynamics and active safety systems team of research at the Department of Mechanics and Aerospace Engineering. He was responsible for PoliTO of more than 50 automotive research projects; he has published more than 100 peer-reviewed international papers.

## 1 Introduction

The gradual decline of known oil reserves has resulted in automotive manufacturers seeking alternative propulsion systems to address today's stringent fuel economy and emission standards. Hybrid-Electric Vehicles (HEVs) help meet these objectives by using advanced electrical energy storage and drive systems to complement conventional powertrains that are powered by Internal Combustion Engines (ICEs). The combined system strives to maximise the overall energy conversion efficiency of vehicles while significantly reducing exhaust emissions.

During development and calibration phases of HEV control strategy, it is of crucial importance to assess and optimise the vehicle drivability, that is, the driver perception during manoeuvres such as launch from standstill, tip-in and tip-out, gear shifts, operating mode changes and, more generally speaking, vehicle response to driver and control unit commands (Levine, 2010). In particular, the high torque gradients generated during tip-in and tip-out manoeuvres excite shuffle vibrations, the lowest global torsional mode of the transmission. This low-frequency mode occurs at 2–10 Hz depending on gear ratio. Transmissions and drivelines with large gear backlash are affected by another undesired

phenomenon, generally referred to as shunt, that is, an initial jerk of the vehicle preceding shuffle oscillations. Also the continuity of power transmission to the vehicle is a critical aspect, hence the lack of driving torque at the wheels, called torque hole or torque gap, should be avoided especially during gear shifts and HEV operating mode changes.

Accurate modelling of the vehicle propulsion system is therefore necessary to evaluate performance and fuel economy in early stages of the vehicle development process. In the case of a HEV, the complex interactions between the electrical and mechanical propulsion systems further increase the need for a high-fidelity vehicle model. It is highly desirable to characterise the effects of propulsion system controls on HEV drivability using computer simulation to reduce controller development and calibration effort.

The objective of this paper is to present such a control-oriented HEV drivability model that allows for the prediction of quasi-steady and transient vehicle responses in the low-frequency spectrum (up to 10 Hz). These responses mainly affect the energy consumption and drivability of a hybrid vehicle.[1] Prediction of undesired transient driveline phenomena such as shuffle, shunt, torque holes and response delays is one of the primary objectives of the proposed vehicle model. A number of drivability issues have been previously investigated in conventional drivetrains for pedal tip-in/tip-out (Levine, 2010; Lefebvre et al., 2003) and for gear-shifting in automatic transmissions (Asgari et al., 2006; Clausing et al., 2002; Cho, 1987) and (automated) manual transmissions (Glielmo et al., 2006; Pettersson and Nielsen, 2000). However, additional drivability disturbances may arise in hybrid-electric drivetrains due to the presence of multiple actuators that have different response characteristics and due to the use of hybrid functions such as engine start-stop. The results presented in this paper focus on such HEV specific drivability disturbances.

Modelling of HEVs has been a topic of extensive research (Syed et al., 2006; Rousseau et al., 2006; Lin et al., 2001; Powell et al., 1998). The simulators described in Rousseau et al. (2006) and Lin et al. (2001) are based on quasi-static energy models that are capable of predicting fuel economy and performance for different HEV configurations. The simulators described in Syed et al. (2006) and Powell et al. (1998) have a frequency range comparable to the model presented in this paper. However, these works do not report thorough experimental validation of the models including quasi-static and transient conditions. Also, the models presented in Syed et al. (2006) and Powell et al. (1998) are suited to power-split type hybrid architectures. The main contribution of this paper is the detailed experimental validation of a through-the-road parallel HEV simulator that incorporates a six-speed automatic transmission model.

This paper is organised as follows: Section II presents the architecture of the experimental vehicle. Section III describes the details of the dynamic HEV model. Section IV provides various comparisons of experimental and simulation results obtained from different driving conditions and concluding remarks are made in Section V. Also, a detailed list of the symbols and subscripts used throughout the paper is given in Section VI and the main model parameters are reported in Section VII.

## 2 Experimental vehicle platform

The experimental vehicle is a commercially available mid-sized sports utility vehicle that is converted to an HEV at the Centre for Automotive Research of The Ohio State University. This effort was motivated by the Challenge-X program; a vehicle development competition with

the goals of achieving better fuel economy and lower emissions through the use of advanced propulsion technologies.

The architecture of the experimental vehicle is illustrated in Figure 1. The components that are relevant to the dynamic model are listed as follows:

- a 1.9 L diesel turbocharged ICE
- a 10 kW DC brushless-type belted starter alternator (BSA) coupled to the engine
- a 6 speed automatic transmission to drive the front axle
- a 32 kW AC induction-type electric machine (EM) connected to the rear axle through a fixed-ratio gearbox
- a 300 V nominal nickel-metal hydride battery pack powering both EMs.

The selected configuration allows for a variety of operating modes such as electric launch, engine load optimisation, motor torque assist, regenerative braking and engine start-stop.

**Figure 1** Experimental vehicle configuration

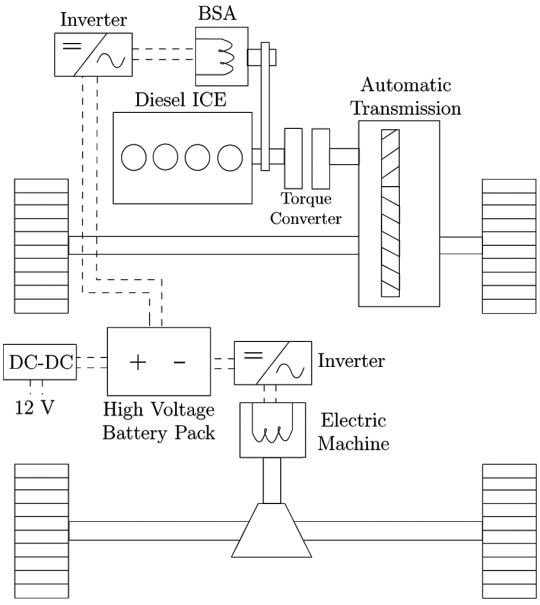


## 3 Model description

A low-frequency dynamic model of the test vehicle is developed to facilitate the evaluation of vehicle drivability, fuel economy and performance. The model is implemented in the MATLAB/Simulink environment using a variable-step solver that is suited for stiff dynamic systems. The following fundamental assumptions are made regarding the vehicle model:

- only longitudinal vehicle dynamics are taken into consideration
- the torsional stiffness of all shafts and gears, except for the rear and front half-shafts, are assumed to be infinitely large

- the frictional properties of the road surface are assumed to be uniformly acting on all tires
- the impacts of environmental factors such as temperature, pressure and humidity are not taken into consideration in the component models
- drivetrain losses are represented by lumped efficiency and viscous friction models.

As a consequence of assumptions 1 and 3, a half car model is used to represent the components downstream from the front and rear differentials. Note that an earlier phase of the dynamic model presented in this paper was described in our previous work (Koprubasi et al., 2007). A description of the individual component models is presented in the below section.

### *3.1 Engine*

The detailed thermodynamic model (Guzzella and Amstutz, 1998) that describes diesel engine dynamics do not provide a substantial amount of additional information for the validation of a drivability-oriented vehicle model. These types of models are often used in the design of engine control systems such as the exhaust gas recirculation valve and the turbocharger. In this work, a simplified engine torque model is used to represent the dynamics between the torque request and the resulting crankshaft speed.

In the test vehicle, the Engine Control Unit (ECU) receives a percentage-based torque request (pedal position or supervisory controller input) and processes this input to generate the actual torque request. A simplified representation of this process is given in Figure 2. The corresponding mathematical expressions can be written as follows:

$$T_{\text{ice,raw}} = f_{\text{ice,raw}}(\omega_{\text{ice}}, T_{\text{ice,per}}) \tag{1}$$

$$\dot{T}_{\text{ice,filt}} = \frac{1}{\tau_{\text{ice,filt}}}(T_{\text{ice,raw}} - T_{\text{ice,filt}}),\ T_{\text{ice,filt}}(0) = K_{\text{ice,filt}} \tag{2}$$

$$T_{\text{ice,req}} = T_{\text{ice,filt}} + T_{\text{ice,idle}} + T_{\text{ice,}tr}. \tag{3}$$

Here, $f_{\text{ice,raw}}$ represents a two-dimensional look-up table, $T_{\text{ice,per}}$ is the percentage-based torque request, $T_{\text{ice,raw}}$ is the raw ICE torque request, $T_{\text{ice,filt}}$ is the filtered torque request and $T_{\text{ice,req}}$ is the actual torque request. $K_{\text{ice,filt}}$ and $\tau_{\text{ice,filt}}$ are filtering parameters that vary

**Figure 2** A simplified illustration of the ECU process that converts a percentage-based torque request into an actual torque request

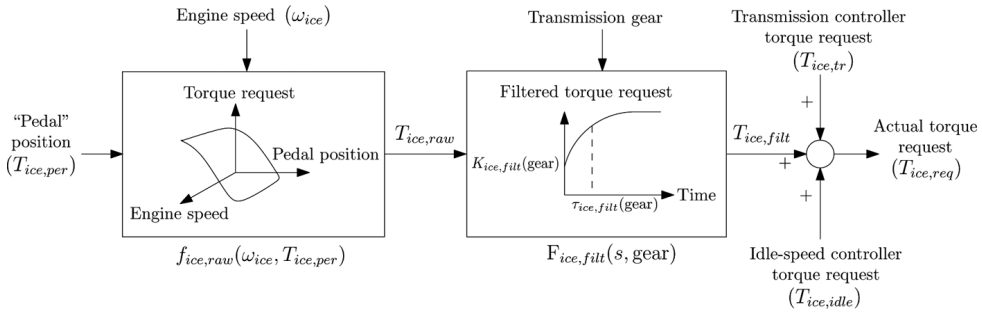

according to the transmission gear ratio. The idle-speed controller ($T_{\text{ice,idle}}$) is modelled as a PI controller combined with a feed-forward term that compensates for the engine friction. The Transmission Control Unit (TCU) torque request ($T_{\text{ice},tr}$) is nominally zero except for gear shifts.
The relationship between the engine torque request and indicated torque is given by

$$\dot{T}_{\text{ice,ind}} = \frac{1}{\tau_{\text{ice}}}(-T_{\text{ice,ind}}(t) + T_{\text{ice,req}}(t - \delta_{\text{ice}})) \tag{4}$$

where $T_{\text{ice,ind}}$ is the indicated engine torque, $\tau_{\text{ice}}$ is the engine time constant due to turbocharger dynamics and $\delta_{\text{ice}} = \pi/\omega_{\text{ice}}$ is the induction-to-power stroke transport delay (180 deg in the crank angle domain). The resulting crankshaft dynamics are given by

$$\dot{\omega}_{\text{ice}} = \frac{1}{J_{\text{ice}} + J_{\text{bsa}} + J_p}(T_{\text{ice,ind}} + T_{bsa} - T_{\text{ice},fr} - T_p) \tag{5}$$

where $J_{\text{ice}}$ is the engine inertia, $J_p$ is the torque converter pump inertia and $J_{\text{bsa}}$ is the combined inertia of the belt, the pulley and the BSA rotor. The mathematical expressions for $T_{\text{bsa}}$ and $T_p$ are given in the following sections. The engine friction is approximated as a quadratic function of the engine speed based on the available engine data:

$$T_{\text{ice},fr} = b_{\text{ice},2}\omega_{\text{ice}}^2 + b_{\text{ice},1}\omega_{\text{ice}} + b_{\text{ice},0}. \tag{6}$$

where $b_{\text{ice},i}$ are engine friction coefficients. All engine accessory loads are lumped into the engine friction. The engine friction also has a strong dependence on the engine temperature. This dependence, which results in a higher friction at low engine temperatures, is not taken into consideration in the engine model. The vehicle model is validated by experiments conducted under moderate engine coolant temperatures (80–100°C).

### *3.2 Torque converter*

The torque converter model is adapted from the empirical quasi-static model developed in Kotwicki (1982). The dynamics due to fluid inertial effects become more pronounced at frequencies higher than 10 Hz (Hrovat and Tobler, 1985). Therefore, these effects are neglected in the torque converter model. The torque converter pump and turbine torques are given as functions of the engine and turbine speeds:

$$T_p(\omega_{\text{ice}}, \omega_t) = \begin{Bmatrix} C_{tc,1}\omega_{\text{ice}}^2 + C_{tc,2}\omega_{\text{ice}}\omega_t + C_{tc,3}\omega_t^2 & 0 \le \omega_t/\omega_{\text{ice}} < \gamma_c \\ C_{tc,4}\omega_{\text{ice}}^2 + C_{tc,5}\omega_{\text{ice}}\omega_t + C_{tc,6}\omega_t^2 & \gamma_c \le \omega_t/\omega_{\text{ice}} \le 1 \\ -C_{tc,4}\omega_{\text{ice}}^2 - C_{tc,5}\omega_{\text{ice}}\omega_t - C_{tc,6}\omega_t^2 & \omega_t/\omega_{\text{ice}} > 1 \end{Bmatrix} \tag{7}$$

$$T_t(\omega_{\text{ice}}, \omega_t) = \begin{Bmatrix} C_{tc,7}\omega_{\text{ice}}^2 + C_{tc,8}\omega_{\text{ice}}\omega_t + C_{tc,9}\omega_t^2 & 0 \le \omega_t/\omega_{\text{ice}} < \gamma_c \\ C_{tc,4}\omega_{\text{ice}}^2 + C_{tc,5}\omega_{\text{ice}}\omega_t + C_{tc,6}\omega_t^2 & \gamma_c \le \omega_t/\omega_{\text{ice}} \le 1 \\ -C_{tc,4}\omega_{\text{ice}}^2 - C_{tc,5}\omega_{\text{ice}}\omega_t - C_{tc,6}\omega_t^2 & \omega_t/\omega_{\text{ice}} > 1 \end{Bmatrix}. \tag{8}$$

$T_p$ and $T_t$ represent the torque converter pump and turbine torques, $C_{tc,i}$ (where $i = 1, \ldots 9$) are empirical coefficients, $\gamma_c$ is the torque coupling speed ratio and $\omega_t$ is the turbine speed. If the torque converter lock-up clutch is engaged, then the torque converter acts as a rigid coupling, that is, $T_p = T_t$ and $\omega_{ice} = \omega_t$.

The torque converter (mechanical) inertial effects are taken into consideration by adding the pump inertia ($J_p$) to the engine side and the turbine inertia ($J_t$) to the transmission input side. This is a reasonable assumption since the transmission input shaft and the engine crankshaft can be assumed as rigid shafts.

### *3.3 Transmission: mechanics*

The six-speed automatic transmission is composed of a series arrangement of a two-stage compound gear set called a Ravigneaux Gear Set (RGS) and a simple Planetary Gear Set (PGS). This arrangement is also known as the LePelletier arrangement (Lepelletier, 1992). The power-flow between the input and output shafts is coordinated by the proper engagement of three wet clutches, two brakes (a band brake and a multi-disc brake) and a single one-way clutch. A layout of the gears, the friction elements and the torque converter is given in Figure 3. This figure also shows the acronyms that are used to refer to the gears and clutches inside the transmission. Figure 4 shows the sign convention adopted for the speeds of the two epicyclic gear trains.

**Figure 3** A stick diagram of the six-speed automatic transmission

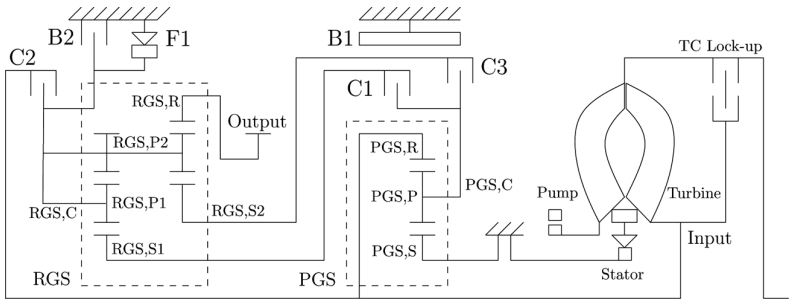


*Source*: Kasuya et al. (2005)

**Figure 4** Sign convention of the epyciclic gear trains

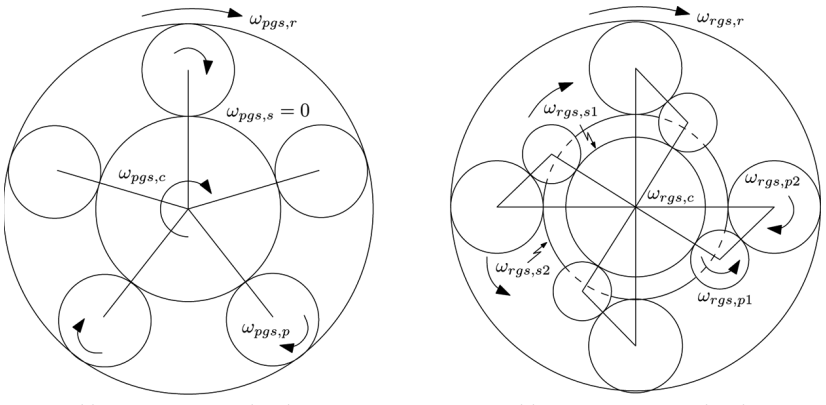


(a)Planetary Gear Set (PGS) (b)Ravigneaux Gear Set (RGS)

The sun gear of the PGS (referred to as PGS,S) is mechanically fixed to the transmission housing. Therefore, the configuration of the PGS imposes the following kinematic constraints:

$$\omega_{\mathrm{pgs},r} = \frac{2R_{\mathrm{pgs},p}}{R_{\mathrm{pgs},r}}\omega_{\mathrm{pgs},p} \tag{9}$$

$$\omega_{\mathrm{pgs},c} = \frac{R_{\mathrm{pgs},r}}{R_{\mathrm{pgs},r} + R_{\mathrm{pgs},s}}\omega_{\mathrm{pgs},r}. \tag{10}$$

$R_{\mathrm{pgs},*}$ are the effective radii of the PGS gears where the subscript * = {$p$, $r$, $s$, $c$} represents the pinion set, the ring gear, the sun gear and the carrier, respectively. The angular speeds of the PGS gears are denoted as $\omega_{\mathrm{pgs},*}$. Similarly, the RGS kinematic constraints can be written as

$$\omega_{\mathrm{rgs},c} = \frac{R_{\mathrm{rgs},p1}}{R_{\mathrm{rgs},c1}K_{\mathrm{rgs},c1} + R_{\mathrm{rgs},c2}K_{\mathrm{rgs},c2}}\omega_{\mathrm{rgs},p1} + \frac{R_{\mathrm{rgs},p2}}{R_{\mathrm{rgs},c1}K_{\mathrm{rgs},c1} + R_{\mathrm{rgs},c2}K_{\mathrm{rgs},c2}}\omega_{\mathrm{rgs},p2} \tag{11}$$

$$\omega_{\mathrm{rgs},s1} = \frac{R_{\mathrm{rgs},c1}}{R_{\mathrm{rgs},s1}}\omega_{\mathrm{rgs},c} - \frac{R_{\mathrm{rgs},p1}}{R_{\mathrm{rgs},s1}}\omega_{\mathrm{rgs},p1} \tag{12}$$

$$\omega_{\mathrm{rgs},s2} = \frac{R_{\mathrm{rgs},c2}}{R_{\mathrm{rgs},s2}}\omega_{\mathrm{rgs},c} - \frac{R_{\mathrm{rgs},p2}}{R_{\mathrm{rgs},s2}}\omega_{\mathrm{rgs},p2} \tag{13}$$

$$\omega_{\mathrm{rgs},r} = \frac{R_{\mathrm{rgs},c2}}{R_{\mathrm{rgs},r}}\omega_{\mathrm{rgs},c} + \frac{R_{\mathrm{rgs},p2}}{R_{\mathrm{rgs},r}}\omega_{\mathrm{rgs},p2} \tag{14}$$

where $R_{\mathrm{rgs},*}$ represent the effective radii of the RGS gears. The subscript * = {$p$l, $p$2, $r$, $s$1, $s$2, $c$} denotes the pinion set 1, the pinion set 2, the ring gear, the sun gear 1, the sun gear 2 and the carrier, respectively. Similarly, $\omega_{\mathrm{rgs},*}$ are the angular speeds of the RGS gears. Note that the subscripts $c$l and $c$2 represent the effective radii of the PGS carrier extending from its axis of rotation to the pinion set 1 and pinion set 2. Also, $K_{\mathrm{rgs},c1}$ and $K_{\mathrm{rgs},c2}$ are constants resulting from the geometric configurations of the pinion set 1 and pinion set 2.

The following kinematic relationships are also valid at the transmission input and output shafts:

$$\omega_t = \omega_{\mathrm{pgs},r} \tag{15}$$

$$\omega_{tr} = \left(\frac{1}{\zeta_{cg}\zeta_{fd}}\right)\omega_{\mathrm{rgs},r} \tag{16}$$

where $\omega_{tr}$ is the transmission output speed and $\zeta_{cg}$ and $\zeta_{fd}$ are the speed reduction ratios of the counter gear and the final drive. Equations (9–14) impose six algebraic constraints (excluding the sun gear constraint, $\omega_{\text{pgs},s} = 0$) on the transmission gear sets, thus resulting in a total of three Degrees of Freedom (DOF). To realise a specific gear ratio, two of these DOFs are constrained by a proper combination of clutches and brakes.

The geometric configurations of the PGS and the RGS are demonstrated in further detail in Figure 4. The pinion arrangement used in the RGS is obtained from Katou et al. (2004). The RGS has two pinion sets (a short pinion set, *P*1 and a long pinion set, *P*2) that are connected to a common carrier. The rotational directions that correspond to the first gear are also shown in Figure 4. In this configuration, clutch *C*1 connects the PGS carrier to the RGS sun gear 1. Also, the one-way clutch *F*1 grounds the RGS carrier to the transmission housing resulting in $\omega_{\text{rgs},c} = 0$.

The following PGS dynamic equations are obtained by computing the net torques about the corresponding gears axes:

$$\dot{\omega}_t = \frac{1}{J_{\text{pgs},1}}(T_t \eta_{tr}\eta_{fd} - T_{tr,fr} - n_{\text{pgs},p} R_{\text{pgs},r} F_{\text{pgs},pr} - T_{c,2}) \tag{17}$$

$$\dot{\omega}_{\text{pgs},p} = \frac{1}{J_{\text{pgs},p}}(R_{\text{pgs},p}(F_{\text{pgs},pr} - F_{\text{pgs},ps})) \tag{18}$$

$$\dot{\omega}_{\text{pgs},c} = \frac{1}{J_{\text{pgs},c}}(n_{\text{pgs},p} R_{\text{pgs},c}(F_{\text{pgs},pr} + F_{\text{pgs},ps}) - T_{c,1} - T_{c,3}). \tag{19}$$

Here, $T_{c,j}$ (where $j = \{1, 2, 3\}$) represent the clutch torques, $J_{\text{pgs},p}$ is the inertia of a single PGS pinion, $J_{\text{pgs},c}$ is the PGS carrier inertia, $n_{\text{pgs},p}$ is the number of gears in the PGS pinion set, $F_{\text{pgs},pr}$ is the reaction force between the pinion and the ring gear and $F_{\text{pgs},ps}$ is the reaction force between the pinion and the sun gear. The inertia at the turbine shaft, $J_{\text{pgs},1}$, can be written as

$$J_{\text{pgs},1} = J_t + J_{\text{pgs},r} + J_{c,2} \tag{20}$$

where $J_{\text{pgs},r}$ is the inertia of the PGS ring gear and $J_{c,2}$ is the combined inertia of the rotating clutch 2 components. $\eta_{tr}$ and $\eta_{fd}$ denote the transmission and final drive mechanical efficiencies. The transmission viscous friction losses, $T_{tr,fr}$, are modelled as a linear function of the turbine speed:

$$T_{tr,fr} = b_{tr,1}\omega_t + b_{tr,0} \tag{21}$$

$b_{tr,0}$, $b_{tr,1}$ are friction coefficients. Note that the efficiency terms $\eta_{tr}$ and $\eta_{fd}$ represent gear meshing losses and they directly multiply the input torque. However, $T_{tr,fr}$ is an additive term that represents the transmission spin losses due to viscous friction.

The differential equations that describe the RGS dynamics are obtained using calculations similar to the PGS:

$$\dot{\omega}_{\mathrm{rgs},s1} = \frac{1}{J_{\mathrm{rgs},2}}(T_{c,1} - n_{\mathrm{rgs},p1} R_{\mathrm{rgs},s1} F_{\mathrm{rgs},s1}) \tag{22}$$

$$\dot{\omega}_{\mathrm{rgs},s2} = \frac{1}{J_{\mathrm{rgs},3}}(T_{c,3} - T_{b,1} - n_{\mathrm{rgs},p2} R_{\mathrm{rgs},s2} F_{\mathrm{rgs},s2}) \tag{23}$$

$$\dot{\omega}_{\mathrm{rgs},p1} = \frac{1}{J_{\mathrm{rgs},p1}}(R_{\mathrm{rgs},p1}(F_{\mathrm{rgs},p2} - F_{\mathrm{rgs},s1})) \tag{24}$$

$$\dot{\omega}_{\mathrm{rgs},p2} = \frac{1}{J_{\mathrm{rgs},p2}}(R_{\mathrm{rgs},p2}(F_{\mathrm{rgs},p2} - F_{\mathrm{rgs},s2} - F_{\mathrm{rgs},r})) \tag{25}$$

$$\begin{aligned}\dot{\omega}_{\mathrm{rgs},c} = \frac{1}{J_{\mathrm{rgs},c}}(&R_{\mathrm{rgs},c1} F_{\mathrm{rgs},s1} + R_{\mathrm{rgs},c2}(F_{\mathrm{rgs},s2} - F_{\mathrm{rgs},r}) \\ &+ K_{\mathrm{rgs},p2} F_{\mathrm{rgs},p2} + T_{c,2} - T_{b,2} + T_{c,f1})\end{aligned} \tag{26}$$

$$\dot{\omega}_{\mathrm{rgs},r} = \frac{1}{J_{\mathrm{rgs},4}}(n_{\mathrm{rgs},p2} R_{\mathrm{rgs},r} F_{\mathrm{rgs},r} - \frac{2}{\zeta_{cg}\zeta_{fd}} T_{hs,f}). \tag{27}$$

$T_{b,k}$ (where $k = \{1, 2\}$) are the brake torques for friction elements B1 and B2, $T_{c,f1}$ is the one-way clutch torque, $J_{\mathrm{rgs},p1}$ is the inertia of a single gear in the RGS pinion set 1, $J_{\mathrm{rgs},p2}$ is the inertia of a single gear in the RGS pinion set 2, $n_{\mathrm{rgs},p1}$ is the number of gears in the RGS pinion set 1, $n_{\mathrm{rgs},p2}$ is the number of gears in the RGS pinion set 2, $F_{\mathrm{rgs},*}$ (where $* = \{s1, s2, p2, r\}$) are reaction forces acting on various gears, $K_{\mathrm{rgs},p2}$ is a constant resulting from the geometric configurations of pinion set 1 and pinion set 2 and $T_{hs,f}$ is the reaction torque of a single half shaft on the front axle. The remaining inertias given in equation (22–27) are the following

$$J_{\mathrm{rgs},2} = J_{\mathrm{rgs},s1} + J_{c,1} \tag{28}$$

$$J_{\mathrm{rgs},3} = J_{\mathrm{rgs},s2} + J_{c,3} \tag{29}$$

$$J_{\mathrm{rgs},4} = J_{\mathrm{rgs},r} + \frac{J_{cg}}{\zeta_{cg}^2} + \frac{J_{fd}}{\zeta_{cg}^2 \zeta_{fd}^2} \tag{30}$$

where $J_{\mathrm{rgs},s1}$ is the RGS sun gear 1 inertia, $J_{\mathrm{rgs},s2}$ is the RGS sun gear 2 inertia, $J_{\mathrm{rgs},r}$ is the RGS ring gear inertia, $J_{cg}$ is the output reflected inertia of the counter gear pair, $J_{fd}$ is the output reflected inertia of the final drive gear set, $J_{c,1}$ is the combined inertia of the rotating clutch 1 components and $J_{c,3}$ is the combined inertia of the rotating clutch 3 components.

The dynamic equations (17–19) and (22–27) are solved together with the kinematic constraints (9–14) to obtain the transmission gear speeds and reaction torques. Note that differential equations (17–19) and (22–27) do not provide a minimal state-space representation of the system since some of the variables are algebraically coupled. The system order can be

reduced by direct substitution of (9–14) into (17–19) and (22–27). However, the resulting closed form expressions become highly complex. Therefore, the solution to the coupled differential-algebraic system is obtained using a numerical iteration method in MATLAB (Shampine et al., 1999). Note that one can further simplify the transmission equations by setting all pinion inertias ($J_{\mathrm{pgs},p}$, $J_{\mathrm{rgs},p1}$, $J_{\mathrm{rgs},p2}$) equal to zero. This would also help improve the computational efficiency of the simulator.

### *3.4 Transmission: hydraulics*

Figure 3 shows the configuration of hydraulically operated friction clutches and brakes as well as the mechanical one-way clutch. These friction elements are activated according to the clutch schedule given in Table 1 (Kasuya et al., 2005). Note that only sequential gear shifts are considered in the vehicle model while neglecting skip shifts such as a 4–6 gear shift. As Table 1 indicates, every upshift or downshift requires the engagement of an on-coming clutch as well as the disengagement of an off-going clutch. A selected friction element remains engaged during a particular gear shift. For example, during a 3–4 upshift, friction element *C*2 becomes engaged, *C*l remains engaged and *C*3 is gradually disengaged.

The dynamics between the clutch pressure commands and the reaction torques generated by the friction elements are fairly involved (Zheng, 1999). In this work, the dynamics between the pressure command and the pressure acting on a clutch actuator are represented by the following second-order transfer function

$$\frac{p_{\star}(s)}{p_{\star,\mathrm{req}}(s)} = \frac{1}{(\tau_{\star,1}s+1)(\tau_{\star,2}s+1)} \tag{31}$$

where $\tau_{*,1}$ and $\tau_{*,2}$ are time constants, $p_*$ is the actual clutch pressure and $p_{*,\mathrm{req}}$ is the clutch pressure request. The subscript $* = \{\{c, 1\}, \{c, 2\}, \{c, 3\}, \{b, 2\}\}$ is used to represent all disc-type friction elements. The clutch torques and the multi-disc brake torque are modelled as functions of the clutch pressures and slip speeds (Zheng, 1999):

$$T_* = p_* A_* n_* R_* \mu_*(\Delta\omega_*) \tanh\left(\frac{\Delta\omega_*}{\omega_{*,th}}\right). \tag{32}$$

**Table 1** Schedule of active friction of elements in different gears (X: engaged). Gear ratios exclude the final drive and counter gear reduction ratios

| *Gear* | *C1* | *C2* | *C3* | *B1* | *B2* | *Fl* | *Gear ratio* |
|---|---|---|---|---|---|---|---|
| 1 | X | | | | | X | 4.148 |
| 2 | X | | | X | | | 2.370 |
| 3 | X | | X | | | | 1.556 |
| 4 | X | X | | | | | 1.115 |
| 5 | | X | X | | | | 0.859 |
| 6 | | X | | X | | | 0.686 |
| R | | | X | | X | | 3.394 |

In this equation, $A_*$ represents the effective disc area of a friction element, $n_*$ is the number of clutch plates, $R_*$is the effective disc radius, $\Delta\omega_*$ is the relative slip speed and $\omega_{*,th}$ is a threshold speed. The coefficient of friction, $\mu_*(\Delta\omega_*)$, is represented by the following expression:

$$\mu_*(\Delta\omega_*) = \mu_{*,1} + \mu_{*,2}e^{-\mu*,3|\Delta\omega_*|} + \mu_{*,4}\left|\Delta\omega_*\right| \tag{33}$$

where $\mu_{*,i}$ are clutch friction coefficients. The three terms in equation (33), respectively, represent the static friction, Stribeck friction and viscous friction effects (Asgari et al., 2006). The variation of clutch torque with respect to clutch slip speed is shown in Figure 5 for different clutch pressures. The following slip speeds determine the direction of the torques generated by the multi-disc friction elements:

$$\Delta\omega_{c,1} = \omega_{\text{pgs},c} - \omega_{\text{rgs},s1} \tag{34}$$

$$\Delta\omega_{c,2} = \omega_{\text{pgs},r} - \omega_{\text{rgs},c} \tag{35}$$

$$\Delta\omega_{c,3} = \omega_{\text{pgs},c} - \omega_{\text{rgs},s2} \tag{36}$$

$$\Delta\omega_{b,2} = \omega_{\text{rgs},c}. \tag{37}$$

**Figure 5** Variation of the clutch torques with slip speed and applied pressure

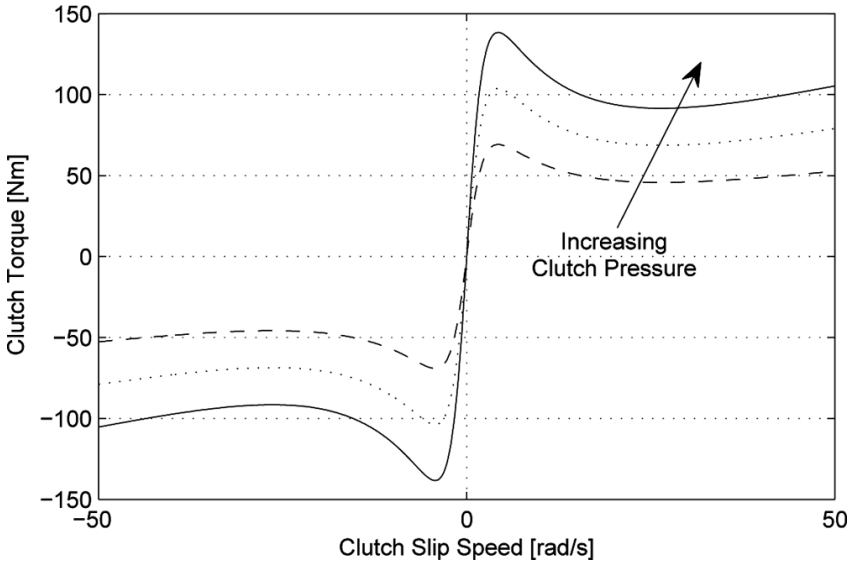

The band brake (*B*l) shows different dynamic behaviour for energising and de-energising engagements (Clausing et al., 2002):

$$T_{b,1} = p_{b,1} A_{b,1} R_{b,1} \cdot \begin{cases} (e^{\mu_{b,1}(\Delta\omega_{b,1})\theta_{b,1}} - 1)\tanh\left(\frac{\Delta\omega_{b,1}}{\omega_{b,1,th}}\right) & \text{for energising engagement} \\ (1 - e^{-\mu_{b,1}(\Delta\omega_{b,1})\theta_{b,1}})\tanh\left(\frac{\Delta\omega_{b,1}}{\omega_{b,1,th}}\right) & \text{for de-energising engagement} \end{cases} . \tag{38}$$

$\theta_{b,1}$ is the band wrap angle, $R_{b,1}$ is the effective band radius, $A_{b,1}$ is the band piston area, $\Delta\omega_{b,1} = \omega_{\text{rgs},s2}$ is the band slip speed and $\omega_{b,1,th}$ is a threshold speed.

The one-way clutch (Fl) only engages in first gear. It allows the RGS carrier to freewheel in one direction while transferring torque in the opposite direction. The one-way clutch dynamics can be represented as

$$T_{c,f1} = \begin{cases} 0 & \text{if} \quad \omega_{\text{rgs},c} > 0 \\ k_{c,f1}\theta_{\text{rgs},c} + b_{c,f1}\omega_{\text{rgs},c} & \text{if} \quad \omega_{\text{rgs},c} \le 0 \end{cases} \tag{39}$$

where $\theta_{\text{rgs},c} = \int \omega_{\text{rgs},c}\,\mathrm{d}t$, $k_{c,f1}$ is the one-way clutch stiffness and $b_{c,f1}$ is the one-way clutch damping coefficient.

The transmission clutch pressure commands are determined on the basis of the transmission line pressure. In this work, the transmission line pressure is assumed to be constant when the engine is running at or above idle speed. In practice, the transmission line pressure is modified by the TCU as a function of parameters such as the engine torque request and the transmission gear.

Furthermore, the vehicle's engine start-stop functionality requires the transmission line pressure to be modified according to the state of the engine since the transmission is pressurised by an engine-driven gear pump. This phenomenon is approximated by the following conditions

$$p_{tr} = \begin{cases} p_{tr,\text{off}} & \text{engine off} \\ f_{tr}(\omega_{\text{ice}})\, p_{tr,\text{on}} & \text{engine cranking} \\ p_{tr,\text{on}} & \text{engine running} \end{cases} \tag{40}$$

where $p_{tr,\text{off}}$ is a small offset pressure, $p_{tr,\text{on}}$ is the nominal transmission line pressure and $f_{tr}(\omega_{\text{ice}})$ is a smoothing function. Note that the transmission line pressure also affects the behaviour of the torque converter during engine start-stop. This dependence is represented in the vehicle model by multiplying the pump and turbine torques by a normalised correction term that is given by $p_{tr}/p_{tr,\text{on}}$.[2]

### *3.5 EMs and rear driveline*

The dynamics of the rear driveline can be described using a lumped model with all inertias reflected to the EM output shaft:

$$\dot{\omega}_{em} = \frac{1}{J_{em} + J_{gb} + \frac{1}{\zeta_{gb}^2} J_{rd}} \left( T_{em}\eta_{gb}\eta_{rd} - T_{em,fr} - \frac{2}{\zeta_{rd}\zeta_{gb}} T_{hs,r} \right) \tag{41}$$

where $J_{em}$ is the EM rotor inertia, $J_{gb}$ is the gearbox inertia on the EM output shaft, $J_{rd}$ is the rear differential inertia on the differential input shaft, $\zeta_{gb}$ is the gearbox speed reduction ratio, $\zeta_{rd}$ is the rear differential speed reduction ratio, $\eta_{gb}$ is the mechanical efficiency of the gearbox, $\eta_{rd}$ is the mechanical efficiency of the rear differential, $T_{em}$ is the EM output torque and $T_{hs,r}$ is the reaction torque of a single half shaft on the rear axle. $T_{em,fr}$ is a friction term that includes all spinning losses in the rear driveline including motor parasitic losses, bearing frictions and alike. $T_{em,fr}$ is modelled as a linear function of the motor speed:

$$T_{em,fr} = b_{em,1}\omega_{em} + b_{em,0} \tag{42}$$

$b_{em,0}$, $b_{em,1}$ are experimentally determined friction coefficients. The mechanical behaviour of the belted-starter alternator is incorporated into the engine crankshaft dynamics given by equation (5). The dynamics of the belt coupling between the engine and the BSA are neglected.

Electrical response characteristics of the EMs are represented by first-order models similar to those used in the engine dynamics. EMs exhibit a short time lag between the torque request and the actual torque output, which can be represented as:

$$\dot{T}_{em} = \frac{1}{\tau_{em}}(-T_{em} + T_{em,\mathrm{req}}) \tag{43}$$

$$\dot{T}_{\mathrm{bsa}} = \frac{1}{\tau_{\mathrm{bsa}}}(-T_{\mathrm{bsa}} + T_{\mathrm{bsa,req}}). \tag{44}$$

$T_{em,\mathrm{req}}$ and $T_{\mathrm{bsa,req}}$ are torque requests received by the EM and the BSA.

### *3.6 Front and rear axles*

In this work, the commonly used linear half-shaft model is extended with a lumped gear backlash model (Lagerberg and Egardt, 2007). This model assumes that the total gear clearance of the front (or the rear) driveline is reflected to the front (or the rear) half-shafts:

$$T_{hs,i} = k_{hs,i}(\theta_{hs,i} - \theta_{bl,i}) + b_{hs,i}(\Delta\omega_{hs,i} - \omega_{bl,i}) \tag{45}$$

The subscript, $i = \{f, r\}$, is used to refer to the front and rear axles,[3] $k_{hs,i}$ is the stiffness of a single half-shaft on axle $i$, $b_{hs,i}$ is the damping coefficient of a single half-shaft on axle $i$, $\Delta\omega_{hs,i}$ is the speed difference between the two ends of a half shaft, $\theta_{hs,i}$ is the torsional displacement on a half-shaft, $\theta_{bl,i}$ is the backlash position and $\omega_{bl,i}$ is the backlash speed. The expressions for half shaft torsional displacement and relative angular speed are given as

$$\dot{\theta}_{hs,i} = \Delta\omega_{hs,i} = \begin{cases} \omega_{tr} - \omega_{wh,f}, & i = f\,(\text{front axle}) \\ \dfrac{1}{\zeta_{gb}\zeta_{rd}}\omega_{em} - \omega_{wh,r}, & i = r\ (\text{rear axle}) \end{cases} \tag{46}$$

where $\omega_{wh,i}$ is the wheel speed. The backlash speed varies as a function of the backlash position (Lagerberg and Egardt, 2007):

$$\dot{\theta}_{bl,i} = \omega_{bl,i} = \begin{cases} \frac{k_{hs,i}}{b_{hs,i}}(\theta_{hs,i} - \theta_{bl,i}) + \Delta\omega_{hs,i}, & |\theta_{bl,i}| < \theta_{bl,0} \\ \max\left(0, \frac{k_{hs,i}}{b_{hs,i}}(\theta_{hs,i} - \theta_{bl,i}) + \Delta\omega_{hs,i}\right), & \theta_{bl,i} = -\theta_{bl,0} \\ \min\left(0, \frac{k_{hs,i}}{b_{hs,i}}(\theta_{hs,i} - \theta_{bl,i}) + \Delta\omega_{hs,i}\right), & \theta_{bl,i} = \theta_{bl,0} \end{cases} . \quad (47)$$

$\theta_{bl,i0}$ represents half of the total gear clearance in the (front or rear) driveline. This equation essentially constrains the backlash position inside a clearance region of $2\theta_{bl,0}$. The extended half-shaft model described by equations (45–47) is also graphically illustrated in Figure 6.

Modelling gear backlash is particularly important for the prediction of rear driveline dynamic behaviour in the test vehicle. The absence of a torque damping device in the rear driveline aggravates drivability issues such as shunt and shuffle that are strongly influenced by gear lash.

**Figure 6** The half shaft model extended with gear backlash. Note that $\omega_{d,i}$, the differential output speed, is equal to $\omega_{tr}$ for the front axle and $\omega_{em}/\zeta_{gb}\,\zeta_{rd}$ for the rear axle

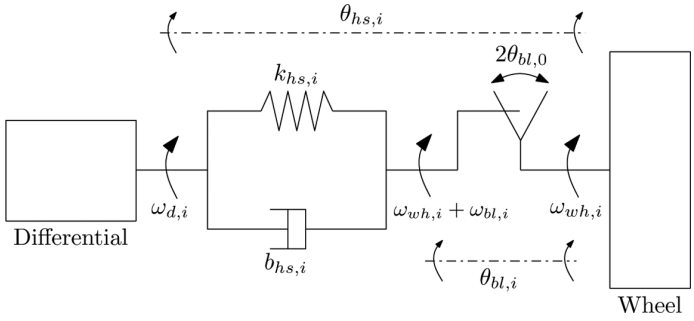


## *3.7 Tires and vehicle*

A nonlinear tire model proposed by Pacejka (2002) is used to represent the longitudinal tire dynamics. This model uses the semi-empirical 'Magic Formula' to compute the tractive forces ($F_{x,i}$) generated by the tires:

$$F_{x,i} = \mu_{wh} F_{z,i} \sin(C_{wh,1} \arctan(C_{wh,2}\kappa'_i - C_{wh,3} (C_{wh,2}\kappa'_i - \arctan(C_{wh,2}\kappa'_i)))). \quad (48)$$

See Figure 7 for a graphical visualisation of the former equation. The Pacejka model coefficients $C_{wh,1}$, $C_{wh,2}$, $C_{wh,3}$ are obtained from the manufacturer's tire data, $\kappa'_i$ is the transient tire slip and $\mu_{wh}$ is the coefficient of friction between the tires and the road surface. The vertical forces acting on the front and rear wheels ($F_{z,f}$ and $F_{z,r}$ ) change as a function of

**Figure 7** Graphical representation of equation (48): longitudinal force $F_{x,i}$ as a function of the transient slip $\kappa_i'$ for different normal loads $F_{z,i}$

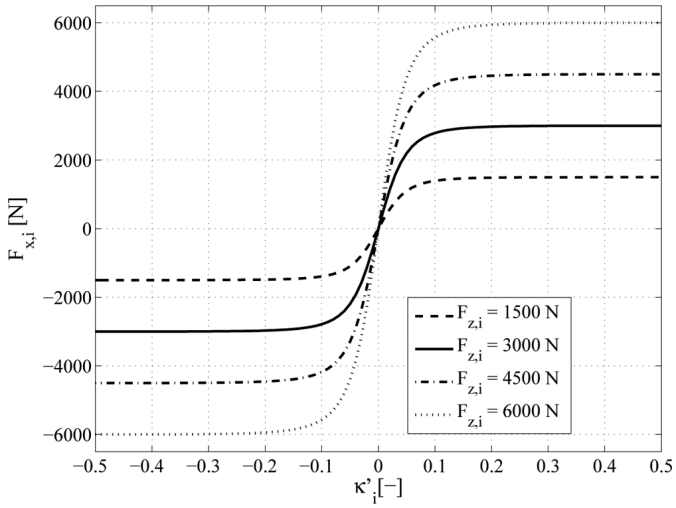


the vehicle acceleration[4] and the resulting longitudinal load transfer can be approximately represented as

$$F_{z,f} = \frac{M_{\text{veh}} g}{4}\left(1 - K_{\text{veh},1}\frac{a_{\text{veh}}}{g} - K_{\text{veh},2}\right) \tag{49}$$

$$F_{z,r} = \frac{M_{\text{veh}} g}{4}\left(1 + K_{\text{veh},1}\frac{a_{\text{veh}}}{g} + K_{\text{veh},2}\right) \tag{50}$$

where $K_{\text{veh},1}$ and $K_{\text{veh},2}$ are geometric vehicle properties, $M_{\text{veh}}$ is the total mass of the vehicle, $g$ is the gravitational acceleration and $a_{\text{veh}}$ is the vehicle's longitudinal acceleration.

As seen in equation (48), transient tire slip $(\kappa_i')$ has a major influence on longitudinal tire force. $\kappa_i'$ is a function of the longitudinal tire deflection, $u_{wh,i}$, which can be computed as

$$\dot{u}_{wh,i} = \begin{cases} 0 & \left|v_{\text{veh}}\right| < v_{\text{veh,low}} \wedge \left|\kappa_i'\right| > 3F_{z,i}/C_{F\kappa} \\ & \wedge\ (v_{s,i} + \left|v_{\text{veh}}\right| u_{wh,i}/\sigma_\kappa) u_{wh,i} < 0 \\ -v_{s,i} - \dfrac{1}{\sigma_\kappa}\left|v_{\text{veh}}\right| u_{wh,i} & \text{otherwise} \end{cases} \tag{51}$$

where the tire slip speed, $v_{s,i}$, is defined as

$$v_{s,i} = v_{\text{veh}} - R_{wh}\omega_{wh,i}. \tag{52}$$

Here, $v_{\text{veh}}$ is the vehicle's longitudinal velocity, $v_{\text{veh, low}}$ is a threshold speed, $\sigma_k$ is the tire relaxation length, $C_{Fk}$ is the longitudinal tire stiffness and $R_{wh}$ is the tire radius under load. The transient slip is then obtained using the following expression:

$$k_i' = \frac{u_{wh,i}}{\sigma_\kappa} - \frac{b_{v,\text{low}}}{C_{F\kappa}} v_{s,i}. \tag{53}$$

The low speed damping coefficient, $b_{v,\text{low}}$, can be computed using an appropriate function such as the one proposed in Pacejka (2002). Using the tire tractive forces and half shaft torques, the wheel speeds are calculated from a torque balance at the wheels:

$$\dot{\omega}_{wh,i} = \frac{1}{J_{wh}}(T_{hs,i} - R_{wh}F_{x,i} - R_{wh}F_{rr,i}) \tag{54}$$

where $J_{wh}$ is the wheel inertia and $F_{rr,i}$ is the tire rolling force. According to the manufacturer's technical specifications, the tire rolling resistance is modelled as a predominantly static function that also has a slight linear dependence on vehicle speed at constant tire pressure:

$$F_{rr,i} = F_{z,i,st}\cos(\gamma)(C_{rr,0} + C_{rr,1}v_{\text{veh}}) \tag{55}$$

where $C_{rr,0}$ and $C_{rr,1}$ are rolling coefficients, $\gamma$is the road inclination and $F_{z,i,st}$ is the static normal load on the tire. Important variables that are used in the tire model are also shown in Figure 8.

**Figure 8** A free-body diagram of the tire

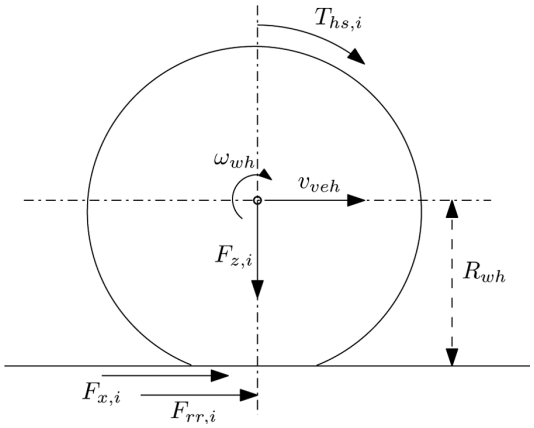


Using the tire forces from the front and rear axles, the longitudinal vehicle velocity can be obtained using the standard vehicle dynamics equation:

$$\dot{v}_{\text{veh}} = \frac{1}{M_{\text{veh}}}(2F_{x,f} + 2F_{x,r} - \frac{1}{2}\rho_a C_d A_{\text{veh}} v^2_{\text{veh}} - M_{\text{veh}} g\sin(\gamma)) \tag{56}$$

where $\rho_a$ is the air density, $C_d$ is the vehicle's drag coefficient and $A_{\text{veh}}$ is the vehicle's frontal area.

### *3.8 High-voltage battery*

The battery model has an indirect influence on vehicle drivability since the battery State-Of-Charge (SOC) (which is a control strategy feedback signal) affects the power-split to the actuators. To predict this effect, a simplified zeroth-order battery model is used to estimate the battery SOC. For information on more sophisticated battery models, the reader is referred to Bornatico et al. (2007).

The power supplied by the battery, $P_{\text{batt}}$, is given as:

$$P_{\text{batt}} = P_{\text{acc}} + \sum_k T_k \omega_k \cdot \begin{cases} \frac{1}{\eta_k(\omega_k, T_k)} & T_k \omega_k \geq 0 \\ \eta_k(\omega_k, T_k) & T_k \omega_k < 0 \end{cases} \quad (k = \{em, \text{bsa}\}) \tag{57}$$

where $P_{\text{acc}}$ is the constant electrical load of the accessories, $\eta_k$ is the combined energy conversion efficiency of the EM (EM or BSA) and its power converter.

The power balance equation together with the Kirchhoff's Voltage Law applied to the battery model allows the computation of the battery current and voltage, knowing the power supplied by the battery ($P_{\text{batt}}$), the estimated battery open-circuit voltage ($V_{oc}$) and the battery internal resistance ($Z_{\text{batt}}$):

$$I_{\text{batt}} = \frac{V_{oc} - \sqrt{V_{oc}^2 - 4 Z_{\text{batt}} P_{\text{batt}}}}{2 Z_{\text{batt}}} \tag{58}$$

$$V_{\text{batt}} = V_{oc} - Z_{\text{batt}} I_{\text{batt}}. \tag{59}$$

The battery internal resistance and the open-circuit voltage are modelled as functions of the battery SOC and these functions vary according to the sign of the battery current. Nominally, these parameters are also affected by the battery temperature. However, the dynamic simulator does not incorporate a thermal battery model and hence, temperature dependence is neglected. Using the battery current and the estimated initial open-circuit voltage, the battery SOC ($S_{\text{batt}}$) can be obtained by direct current integration:

$$S_{\text{batt}}(t) = S_{\text{batt}}(V_{oc}(0)) + \frac{1}{C_{\text{batt}}} \int_0^t I_{\text{batt}} \, \mathrm{d}t \tag{60}$$

where $C_{\text{batt}}$ is the battery energy capacity.

## 4 Experimental validation

The HEV model is validated using a number of longitudinal driving experiments conducted on a dry asphalt surface at nearly zero road grade. Thermal parameters that would normally affect the dynamic behaviour of powertrain components (such as the engine coolant temperature, transmission oil temperature and battery temperature) are monitored such that they are within their nominal (warm) operating ranges.

For the validation of the vehicle model, the control strategy torque commands and the transmission gear command that are recorded from experiments are directly input to the simulator and the desired vehicle states are computed. The primary variables of interest are vehicle acceleration, engine speed, transmission input and output speeds, transmission gear ratio and rear EM speed. Also, the battery pack current and voltage are used for the validation of the battery model. Most of the measurements are logged from the vehicle's controller area network. The longitudinal vehicle acceleration is acquired by a MEMS (Micro Electro-Mechanical System) -type accelerometer that is rigidly mounted on the vehicle chassis.

### *4.1 Electric-only operation*

The first experiment is conducted while the vehicle is in electric-only operating mode, that is, when the vehicle is propelled through the exclusive use of the rear electric motor. Step changes in torque are applied to the rear EM while keeping the engine off. This way the dynamic coupling between the front and rear drive systems is minimised.

Figure 9 shows a comparison of the simulation results and experimental data for the vehicle acceleration and EM speed. Both simulations correlate well with experimental data during transients and quasi-steady operation. Note that the first pedal tip-in at $t = 10$ s causes a larger overshoot in vehicle acceleration compared with the second tip-in at $t = 13$ s, although the torque steps are equal in magnitude ($\Delta T_{em,\mathrm{reg}} = 60$ Nm). This behaviour is a result of the gear backlash and it is accurately captured by the simulator (see Fig. 10(a)).

**Figure 9** Validation of the rear driveline model. The simulated vehicle acceleration and EM speed are compared with experimental data

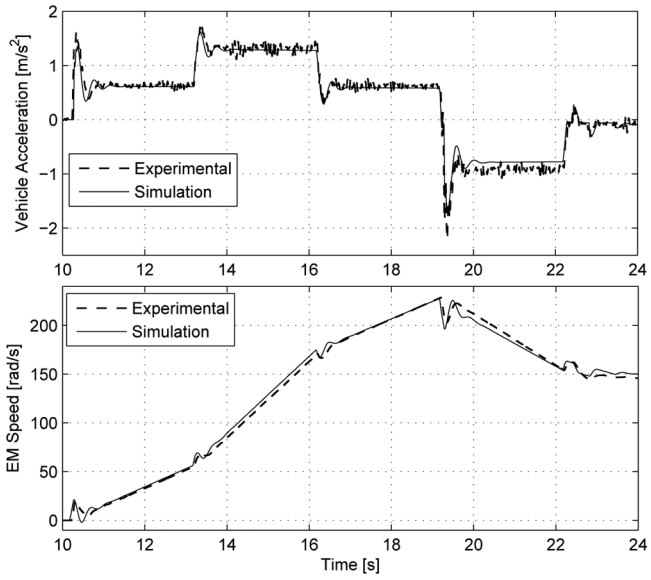


A similar situation arises following the pedal tip-out at $t = 19$ s. Vehicle fore-aft acceleration and gear backlash position (only the simulation result) are shown in Figure 10(b). Note that the pedal tip-out manoeuvre at $t = 19$ s (a pedal tip-out followed by a negative torque

**Figure 10** Detail of the test shown in Figure 9. The gear backlash model accurately represents the transient effects in the rear driveline

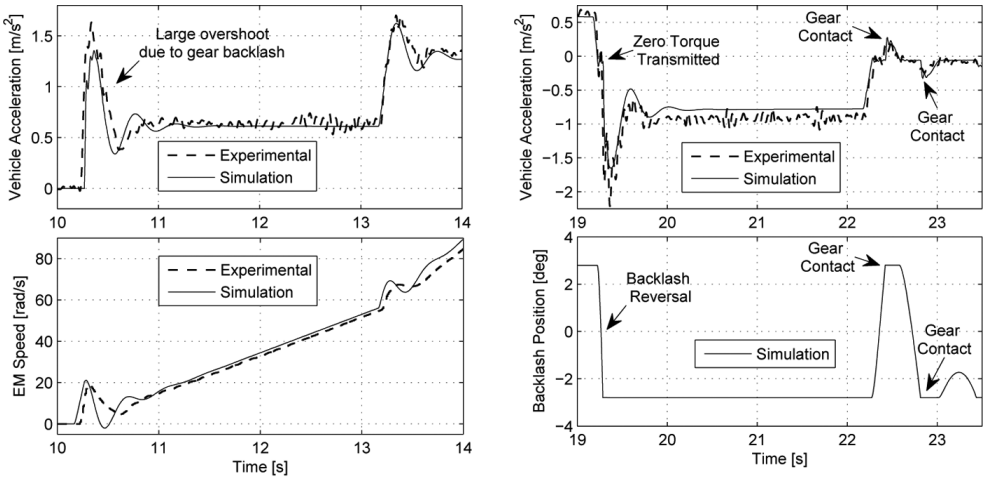


(a)t = 10-14 s (b)t = 19-23.5 s

demand) causes a momentary response delay during backlash reversal followed by a large undershoot in vehicle acceleration. Both transients are accurately predicted by the vehicle model. Another interesting result is seen when the EM torque command changes from –60 to 0 Nm shortly after $t = 22$ s. The driving gear briefly contacts the upper and lower bounds of the gear clearance as a result of the sign change in half shaft torque. The simulation result closely follows the experimental data in this case.

Figure 11 shows a comparison of the simulation results and experimental data for battery model validation. The simulated battery current is in agreement with the experimental data. However, the predicted battery voltage is slightly different than its experimental counterpart. Also, the battery output voltage at $t = 10$ s (with zero current) does not correspond to the open-circuit voltage of the battery since the battery was not sufficiently relaxed prior to the experiment. This issue contributes to the uncertainties in the battery model. However, the same qualitative trend is observed between the two voltage traces despite the visible differences in magnitude. Since the accuracy of the battery model mostly affects fuel economy predictions, the results obtained here are satisfactory for the validation of a drivability-oriented vehicle model.

### *4.2 Engine-only operation*

Another test is conducted to validate the front driveline model while keeping the vehicle in engine-only operating mode; the rear electric motor and the BSA are shut off during the whole duration of the test. The accelerator pedal is maintained at a nearly fixed position during this test. The indicated engine torque that is estimated by the ECU is used as an input to the vehicle simulator. The engine is initially in idle operating condition. Two gear upshifts are commanded by the TCU during the acceleration manoeuvre.

The simulated vehicle states are compared with experimental data in Figures 12 and 13. Vehicle acceleration is considered to be the primary indicator of model accuracy. Other driveline variables of interest are engine speed, torque converter turbine speed (transmission

**Figure 11** The simulated battery pack voltage and current are compared with experimental data for the test shown in Figure 9

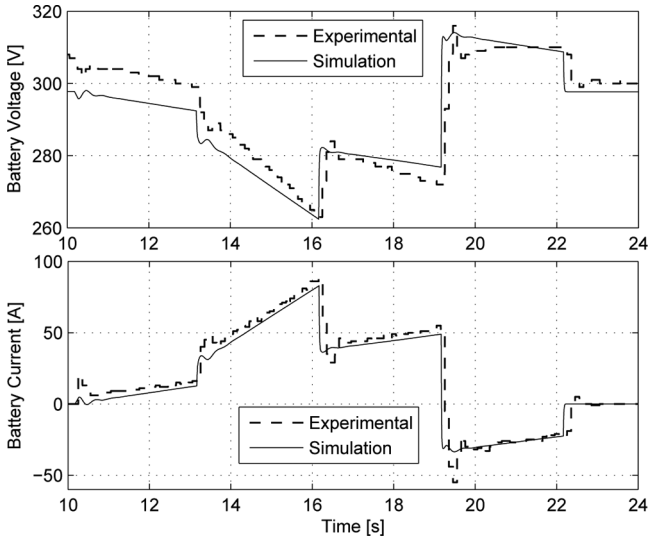


input speed) and transmission output speed. The simulation outputs correlate well with experimental data for both steady and transient conditions. However, the simulated engine speed slightly overestimates experimental data for the majority of the test. Further work is needed to estimate engine friction and torque converter model coefficients with higher accuracy to improve the steady-state prediction capability of the model.

It is clear from Figures 12 and 13 that the most important transients during engine-only operation of the test vehicle are transmission gear shifts. Other disturbances such as driveline

**Figure 12** Validation of the front driveline model in engine-only operation. The simulated vehicle acceleration and engine speed are compared with experimental data

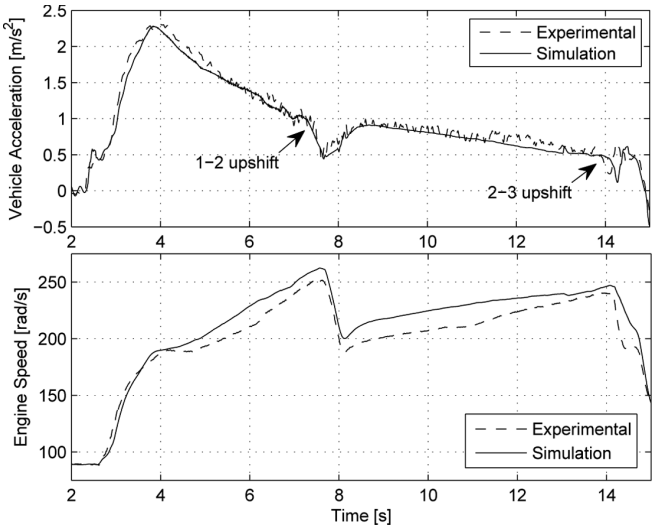

**Figure 13** Validation of the front driveline model in engine-only operation. The simulated transmission input–output speeds are compared with experimental data

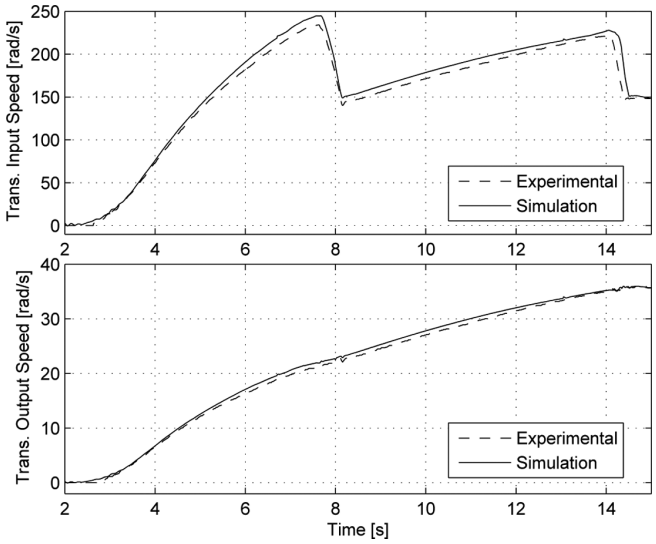


shuffle (as a result of pedal tip-in/tip-out) are not observed in the tests since the excitation frequencies in the vicinity of the fundamental natural frequency of the front driveline are highly damped by the torque converter.

The 1–2 and 2–3 gear shifts are shown in more detail in Figure 14. The primary objective for the validation of gear shift transients is to capture the qualitative behaviour in vehicle acceleration and transmission input/output speeds.[5] The actual transmission behaviour is difficult to capture with reasonable accuracy for all possible gear shifting conditions

**Figure 14** Details of the engine-only operation validation test showing two gear upshifts under medium engine load

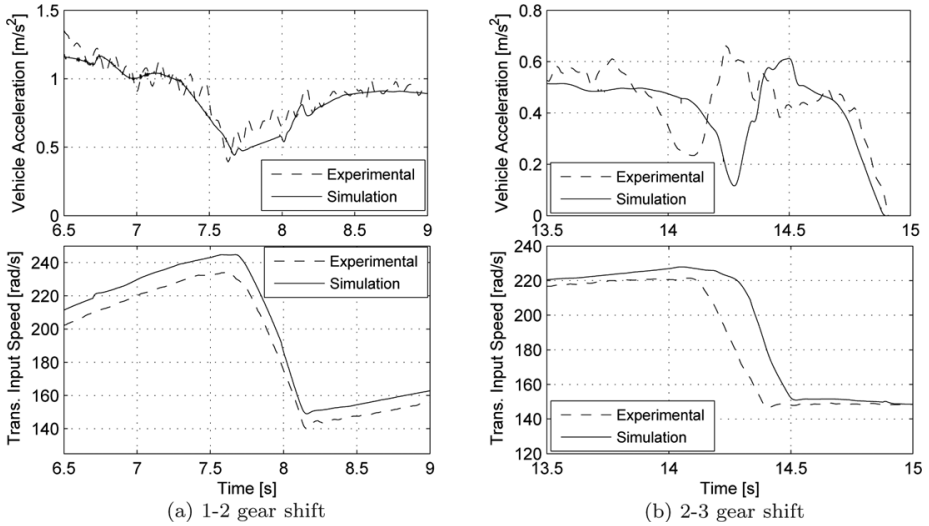


(a) 1-2 gear shift (b) 2-3 gear shift

since some of the physical parameters of the transmission, such as clutch/brake friction coefficients, are not available as measurements. Therefore, representative values are obtained from external resources (Asgari et al., 2006; Clausing et al., 2002; Cho, 1987). Also, note that the clutch pressure traces are slightly calibrated to obtain the results shown in Figure 14. It is difficult to achieve the same level of accuracy in another test conducted under different operating conditions (e.g., with high engine load).

### *4.3 Hybrid vehicle operation*

After the validation of individual driveline models, the overall HEV model is validated during an acceleration that involves a series of operating mode changes. In this test, the vehicle is accelerated from rest using the rear EM. The engine is initially shut off. Under appropriate driving conditions, the engine is started using the belted-starter alternator. Following the engine start, the vehicle advances into hybrid operating mode and it is further accelerated using a proper combination of torques generated by the engine and the two EMs. This is a typical driving condition for the test vehicle. Therefore, accurate prediction of this driving condition is particularly important from a control design standpoint.

The focus of the hybrid mode validation test is the engine start event. The engine start event, if not carefully controlled, results in a torque disturbance that occurs immediately after the first fuel injection (around idle speed).

The severity of this torque disturbance is related to the synchronisation of the two sides of the on-coming clutch.

Various comparisons of the simulation results and experimental data are given in Figures 15–17 for the hybrid mode validation test. Figure 15 shows the vehicle acceleration and the engine speed and Figure 16 shows the transmission input and output speeds. The vehicle

**Figure 15** Validation of the HEV model in hybrid operation. The simulated vehicle acceleration and engine speed are compared with experimental data

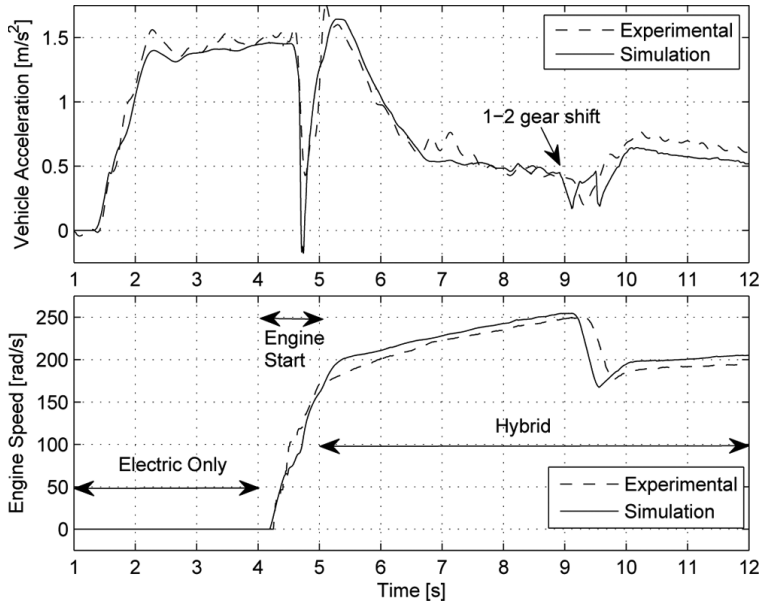

mode changes and the beginning of the 1–2 gear shift are marked on Figure 15. Battery voltage and current are also shown in Figure 17.

**Figure 16** Validation of the HEV model in hybrid operation. The simulated transmission input–output speeds are compared with experimental data

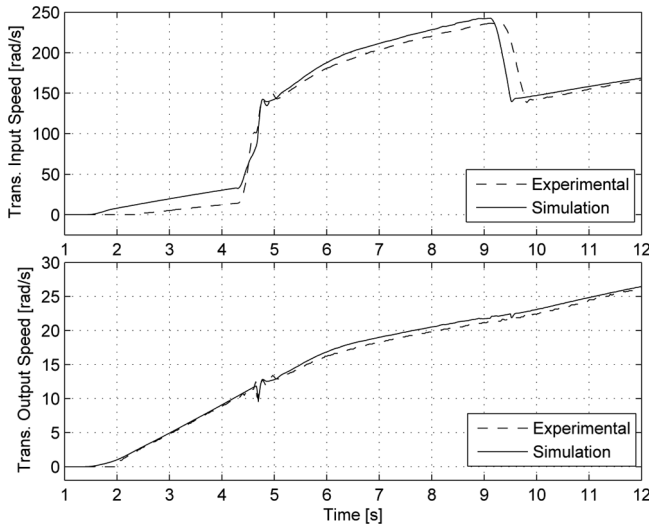


**Figure 17** Validation of the HEV model in hybrid operation. The simulated battery pack voltage and current are compared with experimental data

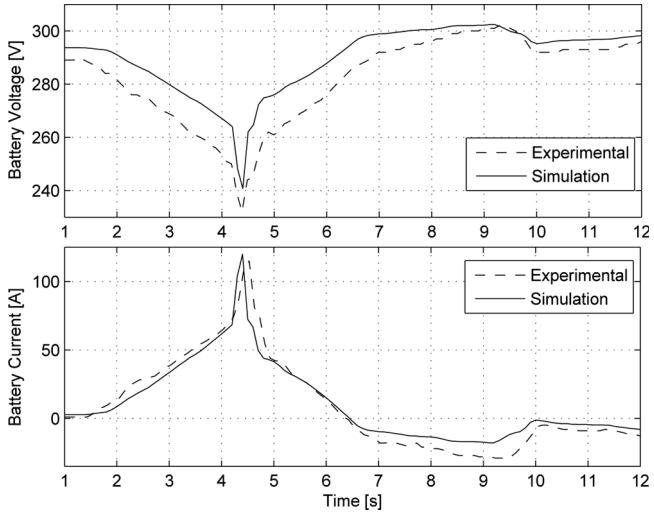


The simulation results and experimental data are in overall agreement as expected from the previous validation tests. However, although details of the gear shift event are not shown here, the simulated acceleration trace does not follow the experimental data as closely as in the engine-only validation case. This result is expected since the clutch pressure

commands used in the engine-only validation test are used here without any modifications. As discussed earlier, this is a crude approximation of the gear shift control algorithm. Therefore, repeatability of this assumption is not high for the purpose of gear shift model validation.

Details of the engine start event are shown in Figure 18. The BSA starts to crank the engine approximately at $t = 4.3$ s. At this time, the engine torque disturbances are not transferred to the wheels since the transmission oil pressure is fairly low. Following the first fuel injection, the transmission oil pressure quickly rises to its nominal value since the actuation mechanism activates after the engine start.[6] As a result, a severe torque hole occurs at $t = 4.7$ s as shown in Figure 18(a). The torque disturbance may appear as a torque rise or a torque hole depending on the sign of the slip speed of the engaging clutch. The angular velocities of the input and output sides of the engaging clutch are shown in Figure 18(c). Only the simulation results are given here since no speed feedback is available from the gears inside the transmission. In this case, a significant amount of jerk is transferred to the wheels because of the uncontrolled engagement of the on-coming clutch.

Figure 18(a) indicates that the magnitude of the simulated jerk is slightly larger than the experimental result. Figure 18(b) confirms this observation since the simulated transmission output speed also drops more than the measured speed at $t = 4.7$ s. However, the difference in magnitude between the simulated and measured speeds does not correlate well with the difference between the simulated and measured vehicle accelerations. This inconsistency is caused most likely due to signal processing. The vehicle acceleration signal contains a significant amount of measurement noise. Therefore, it is low-pass filtered during data

**Figure 18** Details of the hybrid operation validation test highlighting the driveline disturbance that occurs after the engine start

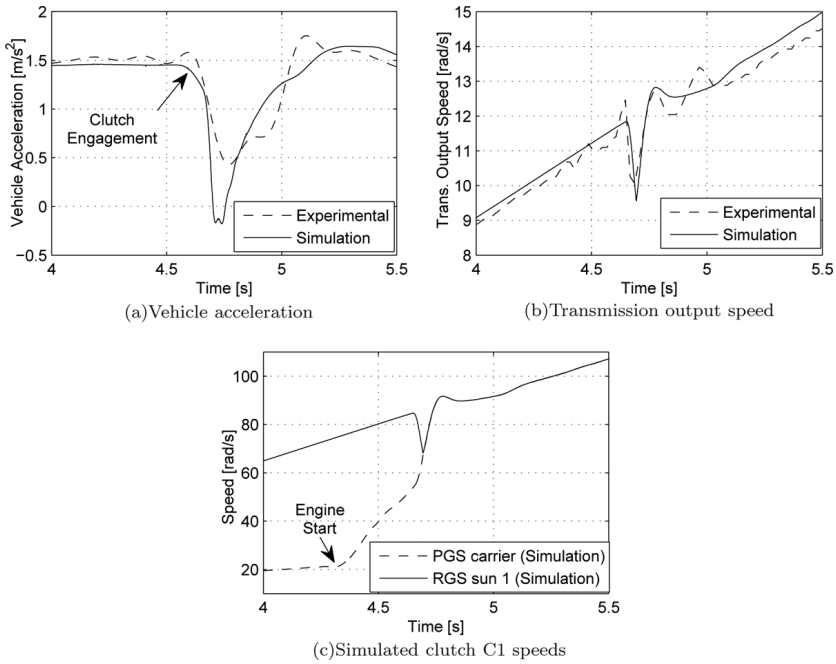


(a)Vehicle acceleration

(b)Transmission output speed

(c)Simulated clutch C1 speeds

acquisition. As a result, some of the abrupt variations in vehicle acceleration, such as the one shown here, are partially rejected by the low-pass filter.

Another discrepancy between the experimental data and simulation result is observed immediately after the clutch engagement (between $t = 4.8$ s and 5 s). The transient response of the simulated transmission output speed is highly damped as shown in Figure 18(b). This artificial smoothing effect is due to the use of a hyperbolic tangent function to represent the clutch torque around zero slip speed.

In this section, graphical comparisons of the simulation results and experimental data are presented for various driving conditions. Although a numerical measure of error may help quantify the accuracy of the simulator in an objective fashion, it may also lead to inaccurate conclusions as a result of the difficulty of aligning transient events in the time domain. For example, an accurately modelled gear shift event such as the one shown in Figure 14(b) may yield to a poor error metric since the experimental and simulated time traces are not properly synchronised.

## 5 Conclusions

This paper demonstrates the development and experimental validation of a low-frequency dynamic HEV model that is suited for the evaluation of vehicle drivability and energy consumption. The vehicle model mainly focuses on the driveline dynamics while the dynamics of the hybrid powertrain actuators (the diesel engine, the EMs and the transmission hydraulic actuators) are simplified. Comparisons of the simulation results and experimental data for electric-only, engine-only and hybrid driving modes confirm that the simulator accurately represents the actual vehicle behaviour during steady and transient operating conditions.

One of the contributions of this paper is the development of a six-speed automatic transmission that also accommodates for the transmission behaviour during engine start-stop. Also, a detailed dynamic model of a through-the-road parallel HEV of the described configuration and its experimental validation are not available in the public domain to the authors' knowledge.

Future work will focus on deriving physics-based models of the hybrid powertrain actuators. This would help improve the fidelity of the vehicle model during transients such as pedal tip-in/tip-out and gear shifts. Also, incorporating a computationally efficient clutch model (such as the one proposed in the study by Karnopp (Karnopp, 1985)) would significantly improve the execution speed of the simulator.

## References

Asgari, J., Deur, J. and Hrovat, D. (2006) 'Modeling and analysis of automatic transmission engagement dynamics-nonlinear case including validation', *ASME Journal of Dynamic Systems, Measurement and Control*, Vol. 128, pp.251–262.

Bornatico, R., Storti, A., Zappavigna, A., Mandrioli, L., Guezennec, Y. and Rizzoni, G. (2007) *NiMH Battery Characterization and State-of-Charge Estimation for HEV Applications*, *in Proceedings of the IMECE*, number 42484.

Cho, D-I. (1987) 'Nonlinear control methods for automotive powertrain systems', *PhD thesis, Mechanical Engineering Department, Massachusetts Institute of Technology (MIT)*, Cambridge, MA, USA.

Clausing, E.M., Megli, T.W., Fujii, Y., Tobler, W.E. and Haghgooie, M. (2002) 'Application of dynamic band brake model for enhanced drivetrain simulation', *Proceedings of the I MECH E Part D, Journal of Automobile Engineering*, Vol. 216, No. 11, pp.873–881.

Glielmo, L., Iannelli, L., Vacca, V. and Vasca, F. (2006) 'Gearshift control for automated manual transmissions', *IEEE/ASME Transactions on Mechatronics*, Vol. 11, No. 1, pp.17–26.

Guzzella, L. and Amstutz, A. (1998) 'Control of diesel engines', *IEEE Control Systems Magazine*, Vol. 18, pp.53–71.

Hrovat, D. and Tobler, W.E. (1985) 'Bond graph modeling and computer simulation of automotive torque converter', *Journal of Franklin Institute*, Vol. 319, pp.93–114.

Karnopp, D.C. (1985) 'Computer simulation of stick-slip friction in mechanical dynamic systems', *ASME Journal of Dynamic Systems, Measurement and Control*, Vol. 107, pp.100–103.

Kasuya, S., Taniguchi, T., Tsukamoto, K., Hayabuchi, M., Nishida, M., Suzuki, A. and Niki, H. (2005) 'AISIN AW new high torque capacity six-speed automatic transmission for FWD vehicles', *in SAE Proceedings, number 2005-01-1020*, pp.1–9, Detroit, MI, USA.

Katou, N., Taniguchi, T., Tsukamoto, K., Hayabuchi, M., Nishida, M. and Katou, A. (2004) 'AISIN AW new six-speed automatic transmission for FWD vehicles', *in SAE Proceedings, number 2004-01-0651*, pp.1–6, Detroit, MI, USA.

Koprubasi, K., Westervelt, E.R., Rizzoni, G., Galvagno, E. and Velardocchia, M. (2007) 'Experimental validation of a model for the control of drivability in a hybrid-electric vehicle', *Proceedings of the IMECE, number 41489*, pp.1–10, Seattle, WA, USA.

Kotwicki, A.J. (1982) *Dynamic Model for Torque Converter Equipped Vehicles*, in *SAE Proceedings*, number 820393.

Lagerberg, A. and Egardt, B. (2007) 'Backlash estimation with application to automotive powertrains', *IEEE Transactions on Control Systems Technology*, Vol. 15, No. 3, pp.483–493.

Lefebvre, D., Chevrel, P. and Richard, S. (2003) 'An h-infinity-based control design methodology dedicated to the active control of vehicle longitudinal oscillations', *IEEE Transactions on Control Systems Technology*, Vol. 11, No. 6, pp.948–956.

Lepelletier, P.A.G. (1992) *Multispeed Automatic Transmission for Automobile Vehicles*, United States Patent: US 5106352.

Levine, W.S. (2010) *The Control Handbook*, Second ed., Control System Applications, CRC Press, Print ISBN: 978-1-4200-7360-7, eBook ISBN: 978-1-4200-7361-4.

Lin, Z., Filipi, C.C., Wang, Y., Louca, L., Peng, H., Assanis, D. and Stein, J. (2001) *Integrated, Feed-Forward Hybrid Electric Vehicle Simulation in Simulink and Its Use for Power Management Studies*, in *SAE Proceedings*, number 2001-01-1334.

Pacejka, H.B. (2002) *Tyre and Vehicle Dynamics*, Butterworth-Heinemann, Oxford, UK.

Pettersson, M. and Nielsen, L. (2000) 'Gear shifting by engine control', *IEEE Transactions on Control Systems Technology*, Vol. 8, No. 3, pp.495–507.

Powell, B.K., Bailey, K.E. and Cikanek, S.R. (1998) 'Dynamic modeling and control of hybrid electric vehicle powertrain systems', *IEEE Control Systems Magazine*, Vol. 18, No. 5, pp.17–33.

Syed, F.U., Kuang, M.L., Czubay, J. and Ying, H. (2006) 'Derivation and experimental validation of a power-split hybrid electric vehicle model', *IEEE Transactions on Vehicular Technology*, Vol. 55, No. 6, pp.1731–1747.

Rousseau, A., Sharer, P., Pagerit, S. and Duoba, M. (2006) *Integrating Data, Performing Quality Assurance and Validating the Vehicle Model for the 2004 Prius Using PSAT*, SAE Proceedings, number 2006-01-0667.

Shampine, L.F., Reichelt, M.W. and Kierzenka, J.A. (1999) 'Solving index-I DAEs in Matlab and Simulink', *SIAM Review*, Vol. 41, pp.538–552.

Zheng, Q. (1999) 'Modeling and control of power-trains with stepped automatic transmissions', *PhD thesis, The Ohio State University*, Columbus, OH, USA.

## Notes

[1]In this work, drivability is regarded as the drive quality perceived by the driver that can be evaluated starting from the vehicle longitudinal acceleration time-history.

[2]Note that this is a crude approximation since the empirical torque converter model is only valid for engine speeds higher than the idle speed.

[3]In the remainder of this section, the subscript i is used to differentiate between the front and rear drive-line components (axles, brakes and wheels).

[4]The effect of the aerodynamic resistance on the longitudinal load transfer is neglected.

[5]Only the details of the transmission input speed are shown here since the transmission output speed does not have enough resolution to facilitate such comparison.

[6]The transmission line pressure is controlled by an engine driven gear pump.

## Nomenclature

| *Symbols* | |
|---|---|
| $A$ | Surface |
| $a$ | Acceleration |
| $b$ | Damping coefficient |
| $C$ | Model coefficient |
| $F$ | Force |
| $f$ | Mapping function |
| $g$ | Gravitational acceleration |
| $I$ | Current |
| $J$ | Inertia |
| $K$ | Geometrical constant |
| $k$ | Torsional stiffness |
| $M$ | Mass |
| $n$ | Number of elements |
| $P$ | Power |
| $p$ | Pressure |
| $R$ | Radius |
| SOC | Battery state-of-charge |
| $T$ | Torque |
| $u$ | Longitudinal tire deflection |
| $V$ | Voltage |
| $v$ | Velocity |
| $Z$ | Resistance |
| $\alpha_{dr}$ | Accelerator pedal position |
| $\beta_{dr}$ | Brake pedal position |
| $\delta$ | Time delay |
| $\eta$ | Energy conversion efficiency |
| $\gamma$ | Road grade |
| $\gamma_c$ | Torque converter coupling speed ratio |
| $\kappa'$ | Transient tire slip |
| $\mu$ | Friction coefficient |
| $\omega$ | Angular velocity |
| $\sigma_k$ | Tire relaxation length |

| | |
|---|---|
| $\tau$ | Time constant |
| $\rho$ | Density |
| $\theta$ | Angular position |
| $\zeta$ | Speed reduction ratio |
| *Subscripts* | |
| *a* | Air |
| acc | Accessory |
| act | Actual quantity |
| *b*,* | Transmission brake,* |
| *bl* | Backlash |
| batt | High-voltage battery |
| *br* | Brake |
| bsa | Belted-Starter Alternator |
| *c*, * | Transmission clutch, * |
| *cg* | Counter gear |
| *d* | Vehicle drag |
| *dr* | Driver |
| *em* | Electric machine |
| *f* | Front (axle or wheel) |
| *f*1 | One-way clutch |
| *fd* | Front differential |
| *fr* | Friction |
| *gb* | Gearbox |
| *hs* | Half shaft |
| ice | Internal combustion engine |
| ice, *f* | Engine fuel |
| idle | Engine idle condition |
| ind | Indicated quantity |
| *oc* | Open-circuit |
| *p* | Torque converter pump side |
| pgs, *c* | PGS carrier |
| pgs, *p* | PGS pinion gear |
| pgs, *r* | PGS ring gear |
| pgs, *s* | PGS sun gear |
| *r* | Rear (axle or wheel) |
| *rd* | Rear differential |
| req | Requested quantity |
| rgs, *c* | RGS carrier |
| rgs, *p*1 | RGS pinion gear 1 |
| rgs, *p*2 | RGS pinion gear 2 |
| rgs, *r* | RGS ring gear |
| rgs, *s*1 | RGS sun gear 1 |
| rgs, *s*2 | RGS sun gear 2 |
| *rr* | Rolling resistance |
| *t* | Torque converter turbine side |
| *tc* | Torque converter |
| *th* | Threshold value |
| *tr* | Transmission |
| veh | Vehicle |
| *x* | Longitudinal direction |
| *wh* | Wheel (or tire) |
| *z* | Vertical direction |

## Main model data

| *Description* | *Value* | *Unit* |
|---|---|---|
| *Vehicle* | | |
| Vehicle mass (empty) | 1957 | kg |
| Drag coefficient | 0.417 | – |
| Frontal area | 2.86 | $m^2$ |
| Length between CG and front axle | 1.273 | m |
| Length between CG and rear axle | 1.587 | m |
| *Rear EM* (*AC induction*) | | |
| Rated power | 32 | kW |
| Peak power | 67 | kW |
| Stall torque | 190 | Nm |
| Inertia | 0.1 | $kgm^2$ |
| *Belted starter alternator* (*PM synchronous*) | | |
| Rated power | 10 | kW |
| Peak power | 21 | kW |
| Stall torque | 82 | Nm |
| Inertia | 0.003 | $kgm^2$ |
| *IC Engine* (*diesel Inline 4-cylinders*) | | |
| Peak power | 107 at 4000 rpm | kW |
| Peak torque | 317 | Nm |
| Engine and TC pump inertia | 0.185 | $kgm^2$ |
| Rear motor gearbox ratio | 3.8 | – |
| Rear differential ratio | 2.7 | – |
| Transmission gear ratios [I … VI] | [4.148, 2.370, 1.556, 1.155, 0.859, 0.686] | – |
| Transmission final drive | 2.77 | – |
| Half shafts combined stiffness | 6000 | Nm/rad |
| Half shafts combined damping | 100 | Nms/rad |
| Total gear backlash at the rear differential input | 7 | deg |
| *Tire* | | |
| Tire effective radius | 0.339 | m |
| Tire moment of inertia (single) | 2.17 | $kgm^2$ |
| Rolling resistance coefficient (constant term) | 0.01 | – |
| *Tire Pacejka coefficients* | | |
| $C_{wh,1}$ | 1.65 | – |
| $C_{wh,2}$ | $20F_z/(1.65F_z + 0.1)$ | – |
| $C_{wh,3}$ | 1 | – |
| $m_{wh}$ | 1 | – |